Research Article | Vol. 9, No. 12 | 1 Dec 2018 | BIOMEDICAL OPTICS EXPRESS 6116
Biomedical Optics EXPRESS

Broadband hyperspectral stimulated Raman scattering microscopy with a parabolic fiber amplifier source

Benjamin Figueroa,[1] Walter Fu,[2] Tai Nguyen,[1,3] Kseniya Shin,[1,4] Bryce Manifold,[1] Frank Wise,[2] and Dan Fu[1*]

[1]*Department of Chemistry, University of Washington, Seattle, WA 98195, USA*
[2]*School of Applied and Engineering Physics, Cornell University, Ithaca, NY 14853, USA*
[3]*Current address: Department of Chemistry, University of Southern California, Los Angeles, CA 90089, USA*
[4]*School of Medicine, University of Washington, Seattle, WA 98195, USA*
**danfu@uw.edu*

Abstract: Hyperspectral stimulated Raman scattering (hsSRS) microscopy has recently emerged as a powerful non-destructive technique for the label-free chemical imaging of biological samples. In most hsSRS imaging experiments, the SRS spectral range is limited by the total bandwidth of the excitation laser to ~300 cm^{-1} and a spectral resolution of ~25 cm^{-1}. Here we present a novel approach for broadband hsSRS microscopy based on parabolic fiber amplification to provide linearly chirped broadened Stokes pulses. This novel hsSRS instrument provides >600 cm^{-1} spectral coverage and ~10 cm^{-1} spectral resolution. We further demonstrated broadband hsSRS imaging of the entire Raman fingerprint region for resolving the distribution of major biomolecules in fixed cells. Moreover, we applied broadband hsSRS in imaging amyloid plaques in human brain tissue with Alzheimer's disease.

1. Introduction

Optical microscopy has become a fundamental and indispensable tool for biomedical research. Because biological systems are heterogeneous at all scales, chemical imaging capable of probing a vast range of molecules *in situ* is becoming increasingly important [1]. Raman spectroscopy is a powerful technique for non-invasive characterization of biological material through their intrinsic molecular vibrational contrasts. Extending this capability to microscopy, a Raman microscope becomes especially useful for the study of biological samples [2–4]. However, the extremely small cross section of spontaneous Raman scattering, makes it unsuitable for high-speed imaging. To address this limitation, Coherent anti-Stokes Raman scattering (CARS) has been developed, which offers orders-of-magnitude higher sensitivity and video-rate imaging [5–7]. However, it has a well-known nonresonant background problem which originates from a four-wave mixing process that distorts vibrational spectra and causes image artifacts [7,8]. Developments in CARS microscopy have mitigated the nonresonant background problem by optimizing experiment procedures and post-image data processing [9–11]. In particular, broadband CARS microscopy followed by phase retrieval has significantly advanced the capability of CARS imaging [12]. In parallel development, stimulated Raman scattering (SRS) microscopy has emerged as an alternative to CARS as a powerful non-destructive and label-free chemical imaging technique [13–21]. It has shown tremendous potential in detecting tumor margins [22–24], unraveling dysregulated lipid metabolism [25,26], and tracing small molecule metabolites and drugs [27–31]. These capabilities benefit from the high sensitivity of SRS imaging as well as the molecular selectivity of Raman spectroscopy. In both CARS and SRS microscopy, two synchronized, ultrashort laser pulses (pump and Stokes) are focused tightly onto a sample. The energy

#345288 https://doi.org/10.1364/BOE.9.006116
Journal © 2018 Received 10 Sep 2018; revised 17 Oct 2018; accepted 2 Nov 2018; published 8 Nov 2018

Biomedical Optics EXPRESS

difference between the two pulses coherently excites an intrinsic Raman vibrational mode allowing for chemically selective imaging. The growing popularity of SRS microscopy over CARS stems from the fact that, unlike CARS, SRS inherently removes the nonresonant background and has a strict linear relationship with molecular concentration, thus facilitating quantitative chemical imaging [14,21]. In comparison, quantitative CARS through background removal (typically using phase retrieval) is a nontrivial task [8]. However, CARS has a major advantage over SRS in that broadband Raman spectra can be easily acquired at high speed due to its lock-in free detection scheme and resistance to laser intensity noise. In fact, this is one of the major limitations of SRS. High resolution and broadband vibrational spectra are of paramount importance to resolve minute chemical composition variation in biological samples and detect small molecules. To differentiate and quantify different molecules based on their unique vibrational signatures, multiple Raman transitions must be probed with SRS, necessitating the use of multiplex SRS or hsSRS imaging [32–36].

In a typical SRS microscopy setup, transform-limited picosecond lasers with narrow bandwidths, which are less than the Raman line widths (<10 cm^{-1}), are used to probe Raman-active vibrations of interest with high spectral resolution. To probe a different transition, the energy difference between the two pulses must be tuned by changing one of the two wavelengths. This tuning process typically involves changing the crystal temperature or cavity length of the optical parametric oscillator [23,37]. Additionally, only a limited wavelength range can be scanned without time-consuming adjustments. In practice, wavelength tuning of typical laser sources is usually slow and susceptible to optical power and wavelength drifts, which limits the acquisition speed and quantification accuracy of SRS imaging.

Another way to acquire spectroscopic information is to employ a combination of picosecond and femtosecond laser sources. This can be achieved with either a grating based spectrometer or Fourier-transform spectrometer [38,39]. With this method, imaging at 4 μs per spectrum can be achieved, enabling applications in flow cytometry. While pico-femto based SRS imaging approaches work well for simple systems, the complicated instrumentation and limited sensitivity restrain their use mostly to SRS imaging in the C-H imaging for lipids and proteins. One reason for the limited sensitivity is that the optical power is distributed among many Raman vibrational modes so that each Raman transition is less efficient than that of SRS excitation with picosecond lasers.

An alternative approach to SRS excitation with picosecond lasers is SRS imaging with femtosecond lasers and the "spectral-focusing" approach [35,36,40–45]. The spectral focusing approach offers much higher spectral resolution than direct femtosecond laser excitation by sending the pulses through a dispersive medium. This introduces linear chirp through the temporal spreading of the frequency components of the two femtosecond excitation sources, leading to narrower instantaneous bandwidths. Tuning different vibrational frequencies within the range of the broad laser bandwidth is done by simply varying the temporal delay between the two chirped pulses. Early reports have demonstrated the capability of employing the spectral focusing approach for SRS using a femtosecond oscillator and a fiber-generated secondary source [35,41]. However, in these reports, the low power output from the fiber limited the acquisition sensitivity and imaging speed.

In either pico-femto or femto-femto SRS imaging, suitable synchronized laser sources are required. The introduction of the commercial dual output femtosecond lasers such as the Insight DS + (SpectraPhysics) offers a robust and simple solution to the excitation laser requirement. Such systems are advantageous compared to Ti:sapphire and fiber based laser systems because of their simple tuning, high power, and synchronization stability. Thus, it is becoming the leading laser source for hsSRS imaging. The laser outputs a fixed 1040 nm laser with ~60 cm-^{1} bandwidth and a tunable laser with ~150 cm^{-1} bandwidth. In both pico-femto and femto-femto hsSRS configurations, the spectral coverage of SRS is limited by the spectral bandwidths of the laser sources. With Insight DS + , it is limited to <300 cm^{-1}.

Biomedical Optics EXPRESS

Additionally, the spectral resolution of most current systems is limited to ~20-25 cm^{-1} [46,47]. While these capabilities are often sufficient for imaging in the high wavenumber region (2800-3050 cm^{-1}), they are insufficient for imaging in the fingerprint region (700-1800 cm^{-1}).

SRS imaging spanning a large spectral range is under intense technical development. Beier et al. demonstrated the acquisition of a reliable Raman spectrum over a large spectral range using a supercontinuum generated by a photonic crystal fiber as either the pump or the Stokes beam [41]. However, this approach suffers from low signal-to-noise ratio (SNR) due to two reasons: (1) large bandwidth mismatch and (2) low power output from the fiber, which significantly limit the imaging speed to (3 ms/pixel). Most recently, Karpf et al. developed a broadband SRS time-encoded technique using rapidly wavelength-swept continuous wave probe lasers combined with a short-duty-cycle actively modulated pump laser [48]. High speed, broad spectral coverage (750-3150 cm^{-1}) and high resolution were achieved in this, albeit, complex configuration. However, the low power output limited the system's sensitivity and with it the imaging speed to achieve a sufficient SNR (250 μs per spectral point).

In this manuscript, we present a simple and novel approach for broadband hsSRS imaging. based on parabolic pulse amplification, which offers increased spectral range and spectral resolution [49]. It has been shown that propagating an ultrashort pulse through a sufficiently long, normally-dispersive fiber amplifier results in a linearly chirped parabolic pulse, which is the asymptotic self-similar solution of the nonlinear Schrodinger equation with gain [50–53]. In addition, it is within this self-similar regime that the seed pulse spectrum will be significantly broadened due to self-phase modulation. It is important to note, however, that additional higher-order linear or nonlinear effects may occur and ultimately limit the propagation length of the parabolic pulses and/or introduce parasitic effects [54–56]. Nonetheless, numerous studies have performed numerical and experimental studies which provide a series of guidelines in determining the design of fiber amplifiers to operate in the asymptotic parabolic pulse regime [52,53,57,58].

Besides spectral broadening, parabolic amplification has two noteworthy properties: (1) the peak power, duration, and shape of the resulting pulses depend only on the seed pulse energy and (2) the output pulse has nearly perfect linear up-chirp. As a result, linearly chirped pulses with ~50 nm (or 500 cm^{-1}) bandwidth centered around 1050 nm can be readily obtained. In combination with the existing pump pulse provided by the Insight DS + , a 650 cm^{-1} spectral range, a 2-fold increase over our previous system, can be covered by hsSRS without changing laser wavelength. Due to the increased bandwidth, the Stokes laser will also be much longer in pulse duration after chirping, leading to improved spectral resolution. To optimize the spectral resolution, the linear chirp of the pump and the Stokes are matched. We achieve and demonstrate that a maximum spectral resolution of 10 cm^{-1} is possible when the chirps of the excitation beams are properly matched. We then validate the benefit of employing parabolic pulse amplification on our system by the hsSRS imaging of mammalian cells and brain tissue.

2. Materials and methods

2.1 Chemicals and materials

Reagent grade methanol, oleic acid, benzonitrile, nitrobenzene, dimethyl sulfoxide (DMSO), hydrochloride acid, and insulin were all purchased from Sigma-Aldrich (St. Lous, MO) with purity ≥ 95%. Glass slides were purchased from VWR (Radnor, PA). Glass coverslips are from Thermo Scientific (Porthsmouth, NH).

2.1 Cell culture

Human embryonic kidney (HEK293) cells were maintained at 37° C in a humidified 5% (vol/vol) CO_2 air incubator and cultured in DMEM (Invitrogen Carlsbad, CA) supplemented

Biomedical Optics EXPRESS

with 10% (vol/vol) FBS and 1% (vol/vol) penicillin/streptomycin. Before imaging, HEK293 cells were seeded on glass cover slips and fixed with 4% paraformaldehyde (PFA) for 30 minutes.

2.2 Insulin fibrils control samples

10 mg of insulin was placed into 4 ml of HCl. The solution was mixed at 300 rpm in a water bath kept at a constant temperature of 70° C for 18 hours to induce the fibril formation. The final sample was centrifuged for 5 minutes to isolate fibrils from dissolved insulin. The insulin fibril sample was mounted on a glass slide and a coverslip was added prior to imaging.

2.3 Alzheimer's brain samples

Brain tissue from a donor was provided by University of Washington Neuropathology Core, Seattle, WA. A superior temporal gyrus brain tissue was collected less than 8 hours of postmortem interval, fixed in 10% neutrally buffered formalin solution. A cross section through cortex and white matter at ~500 μm was mounted on a glass slide and a coverslip was added prior to imaging.

2.4 Hyperspectral SRS imaging with a parabolic fiber amplifier

A broadband femtosecond dual beam laser system (Insight DS + from Spectra-Physics) was used for hsSRS imaging as described in our earlier publication [46,59]. Figure 1 shows our experimental setup. The Stokes beam is coupled into a 4-m polarization maintaining Yb-doped fiber (YB1200-6/125 DC-PM Thorlabs) with a beam collimator and acts as the seed for laser amplification. An input pulse seed energy of 25 pJ was used for amplification throughout this entire study which ensures convergence to the parabolic regime [51–53,58]. A half wave plate was placed at the input to optimize polarization of the seed pulse transmitting through the fiber. The gain fiber is then pumped in the counter-propagation pumping scheme by a 976-nm high power laser diode (BWT) and combined with the seed using a wavelength division multiplexer with a power rating of 7 W (PMC02112340 IFT Technologies). An electro-optical modulator is then placed in the amplified Stokes beam, modulating at 20 MHz. A motorized delay line is inserted into the Stokes beam to scan the time delay between the pump and the Stokes. After collinearly recombining the two beams through the dichroic mirror DMSP1000 (Thorlabs), the beams were directed in to a home-built laser scanning microscope (NIKON Eclipse FN1). An Olympus microscope objective of 25 × (XLPLN25XWMP2) with 1.05 NA was used to focus the beams onto the samples. On the detection side, the Stokes beam is filtered out by a short–pass filter FESH1000 (Thorlabs), and the pump beam is detected by a 10 × 10 mm^2 silicon photodiode (Hamamatsu) biased at 56 V and then amplified by a home-built transimpedance amplifier. Stimulated Raman loss (SRL) signal is detected with a Zurich Instruments lock-in amplifier (H2FLI). For SRS imaging, the lock-in time constant is at 8 μs and each frame is 512 × 512 pixels with 0.5 frame/sec acquisition speed, unless noted otherwise.

For hsSRS imaging with spectral focusing, the pump beam is chirped by a grating stretcher in quadruple-pass configuration [60,61] while the amplified Stokes pulse is chirped further by 36 cm of high dispersion H-ZF52A glass rods to appropriately match the chirp of the pump beam. To compare the imaging capability of the new laser system versus the old laser system, a spectral-focusing SRS setup with outputs directly from the Insight laser was employed. In this setup, the pump is chirped by 60 cm of high dispersion glass rods, while the Stokes is chirped by a grating stretcher setup.

Biomedical Optics EXPRESS

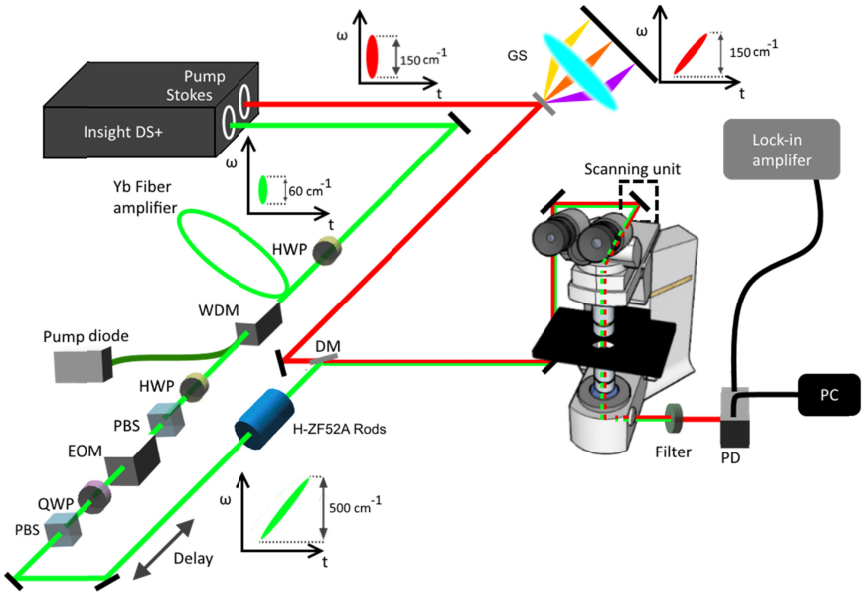

Fig. 1. Schematic diagram of the hsSRS imaging setup based on a femtosecond dual beam laser system. Abbreviations: GS, grating-stretcher; HWP, half waveplate; WDM, wavelength division multiplexer; PBS, polarizing beam splitter; EOM, electro-optical modulator; QWP, quarter waveplate; DM, dichroic mirror; PD, photodiode.

3. Results and discussion

We first measured the pulse properties of the parabolic fiber amplifier output. Seeding the fiber amplifier with 2 mW (25 pJ) of ~280 fs pulses, ensures the generation of linearly chirped parabolic pules which experience large temporal and spectral broadening as can be seen in Fig. 2. From Fig. 2(A) and (B) it is apparent that the spectrum of the amplified Stokes pulses increases in an almost linear fashion with only large amplification showing deviation from linearity (7 W). The ability to tune to different bandwidths solely by changing the 976 nm pump power that is launched into the fiber provides a quick and easy tool for various applications as will be shown later. Likewise, the pulse width of the Stokes pulse significantly broadens from the nearly transform-limited input seed pulse (Fig. 2(B)). Although a linear increase in pulse width is exhibited, an exponential increase in pulse widths is expected from the parabolic output [50–53,58]. We hypothesize that this is due to the addition of the 36 cm of dispersion glass rods used for matching the chirp rates between the pump and Stokes for SRS imaging, and therefore could be masking the exponential increase that is expected. Another additional benefit of employing parabolic amplification is the production of up to 2.5 W average output power which is more than plenty of optical power for hsSRS imaging, which therefore does not experience the limitations characteristic of other broadband SRS setups [35,41,48]. The slope efficiency is about 43% with respect to the absorbed pump power which is shown in Fig. 2(C). With these improvements, increased spectral resolution and spectral coverage is expected due the enlarged pulse width and bandwidth of the Stokes beam.

Biomedical Optics EXPRESS

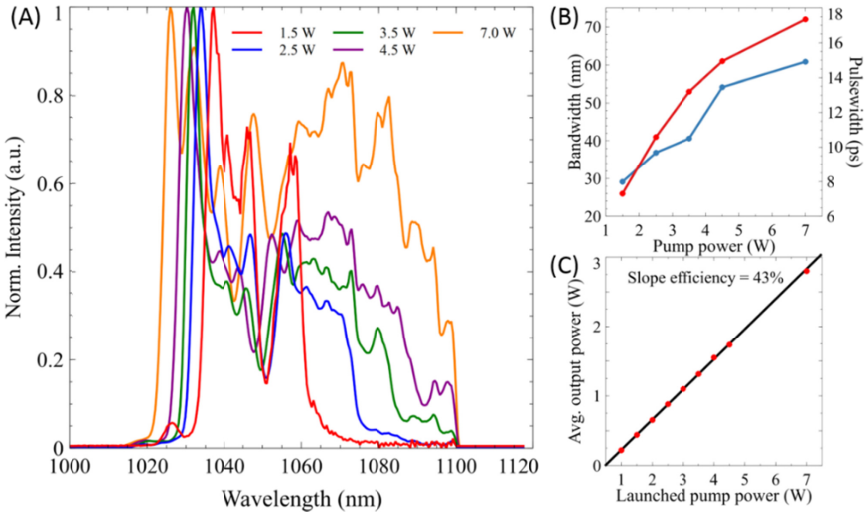

Fig. 2. A) The optical spectra of the Stokes pulse in a parabolic fiber amplifier as a function of launched pump power. B) The bandwidth at FWHM (red) and pulse width (blue) of the amplified pulse after the 36 cm of glass rods as a function of launched pump power. C) Output power characteristics of the parabolic fiber amplifier.

To demonstrate the benefit of employing parabolic pulse amplification for increased SRS spectral coverage, SRS spectra of various organic solvents were taken using the traditional SRS setup and compared with results from the fiber amplifier setup. The spectral region of interest that would most benefit from the increased spectral coverage is the so-called "fingerprint region." Sharp Raman vibrational modes in this region provide particularly valuable information for molecular identification. We first demonstrated the limitations of our previous SRS setup to probe the entire fingerprint region (Fig. 3(A)). We measured the SRS spectra by recording the SRS signal while scanning the interpulse time delay between the pump and the unamplified Stokes beam. The pump beam was tuned to 916 nm to center our probed Raman spectra at 1300 cm^{-1}. Figure 3(A) shows the SRS spectra of oleic acid, nitrobenzene, benzonitrile, and methanol collected with 220 spectral points with each point acquired with a 100 µs pixel dwell time. Here the spectral range is limited by the bandwidth of the femtosecond laser beams to ~300 cm^{-1}. Due to the limited bandwidth of the pump and Stokes lasers, it is evident that tuning of the pump beam to scan throughout the fingerprint region (700 – 1700 cm^{-1}) is unavoidable and requires a minimum of 4 different pump excitation frequencies, with each wavelength change requiring several seconds for stabilization. In addition, the spectral resolution achieved was experimentally determined to be approximately 19 cm^{-1} though a Lorentzian fitting of 1347 cm^{-1} peak of nitrobenzene. For comparison, Fig. 3(B) shows the spectra of these same solvents by employing parabolic amplification of the Stokes pulse, collected under the same imaging parameters as before. To obtain the broadest possible spectral coverage, the Yb-doped fiber was pumped with a power of 7 W, which leads to the Stokes bandwidth being amplified to ~70 nm for a total theoretical coverage of approximately 800 cm^{-1} as shown in Fig. 3(B). Here, we used a pump excitation wavelength of 927 nm, to center our Raman transition at ~1300 cm^{-1}. The spectral resolution achieved with this large bandwidth was approximately 14 cm^{-1}, calculated by Lorentzian fitting of the 1347 cm^{-1} peak of nitrobenzene. However, pumping the gain fiber with high power does not come without its limitations. As can be seen, pumping beyond the fiber's gain bandwidth begins to introduce higher order nonlinear chirp [55,62,63], which distorts the SRS spectra, particularly at lower wavenumbers compared to the spontaneous Raman spectra shown in Fig. 4(B). We note that this might be the reason for the lower than expected spectral

Biomedical Optics EXPRESS

resolution. Nonetheless, this improvement in spectral resolution provides the ability to resolve many closely spaced Raman peaks such as the 1177 and 1192 cm^{-1} peaks from benzonitrile. Thus, careful balance of bandwidth and linearity in spectral resolution should be considered when optimizing for a given experiment. Therefore, operating the parabolic fiber amplifier within the gain bandwidth limit should produce the most optimum experimental condition for SRS microscopy.

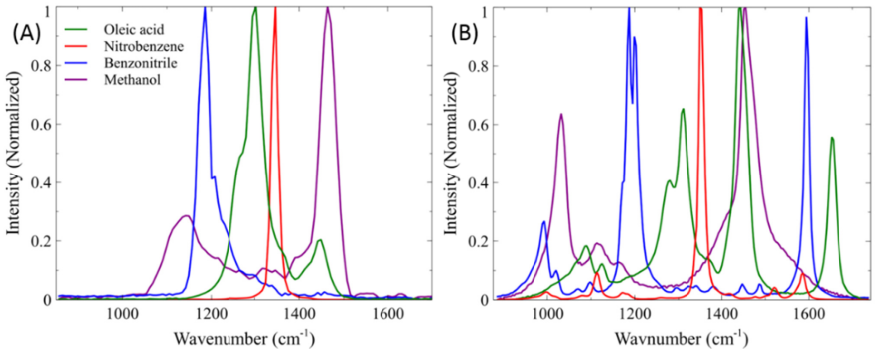

Fig. 3. (A) SRS spectra of organic solvents using 60 cm of high dispersion glass rods and pump wavelength of 916 nm. (B) SRS spectrum of organic solvents using stretcher-grating pair and Yb-doped fiber amplifier pumped at 7 W. I_P and I_S = 40 mW.

To this end, we demonstrated that the entire fingerprint region could be examined with a minimum of two changes in pump excitation wavelength (912 and 949 nm) for optimum spectral resolution, as can be seen in Fig. 4(A). Pumping the gain fiber with a power of 3.5 W for a bandwidth of ~50 nm (500 cm^{-1}) allows us to probe from ~1200 to 1750 cm^{-1}, while pumping at 4.5 W allows for the coverage from 700 to 1200 cm^{-1}. This total spectral coverage was again collected with 240 spectral points with each point acquired with a 100 µs pixel dwell time. For comparison, Fig. 4(B) shows the spontaneous Raman spectra of nitrobenzene, oleic acid, benzonitrile, and methanol by a commercial confocal Raman instrument (Renishaw InVia). It is evident that the SRS and spontaneous Raman spectra are almost identical except for the slightly better spectral resolution than that achieved by our system. The validation of this increase in spectral range is a significant advantage in convenient and rapid hsSRS imaging compared to the multiple wavelength tuning process necessary with standard synchronized femtosecond beams. We demonstrated that with our new laser system, a spectral resolution of ~10 cm^{-1} is achieved, ~2 fold better than the original SRS system.

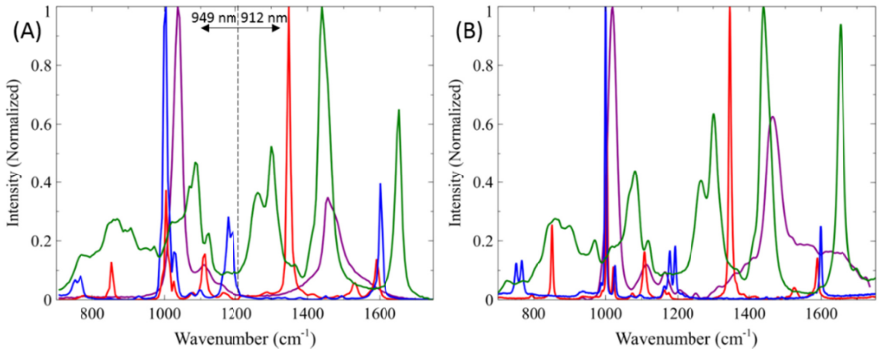

Fig. 4. (A) Stitched SRS spectra of organic solvents covering the entire fingerprint region using two pump wavelengths: 949 nm and 912 nm and the Yb-doped fiber amplifier pumped at 4.5 W and 3.5 W, respectively. I_P and I_S = 40 mW. (B) Spontaneous Raman spectra of organic solvents. Green: oleic acid, red: nitrobenzene, blue: benzonitrile, magenta: methanol.

Biomedical Optics EXPRESS

To demonstrate the capability of the improved hsSRS imaging in biological samples, we imaged PFA fixed HEK293 cells via the traditional glass rod setup and our parabolic fiber amplifier. In most Raman studies of biological samples, the region from 2800 to 3050 cm^{-1} is studied due to the CH_2 stretching vibration of lipids (2850 cm^{-1}) and the CH_3 stretching vibration of proteins (2930 cm^{-1}). Because protein and lipids have distinct SRS spectra in this high wavenumber region, visualization of cell morphology can be readily achieved due to heterogeneous distribution of biomolecules in different cellular compartments. Figure 5(A) shows a SRS frame (512 x 512 pixels) at 2930 cm^{-1} of fixed HEK293 cells using the glass rod setup with an 800 nm pump beam. We imaged PFA fixed HEK293 cells with a total of 45 spectral frames at wavenumbers ranging from 2795 to 3165 cm^{-1} at 0.5 frame/sec with a pixel dwell time of 8 µs. At every single pixel in the frame, a spectrum can be plotted (equivalent to 360 µs per spectral acquisition). Figure 5(C) shows HEK293 cells imaged with the parabolic amplifier pumped at 2.5 W. The Stokes bandwidth is ~40nm, which provides nearly doubled spectral range (510 cm^{-1}) than the original SRS system. This improvement can be readily observed when the SRS spectra of a cell's lipid droplet, nucleus, nucleolus, cytoplasm, and background/water are plotted as points A, B, C, D, and E respectively. Because we acquired a larger range from 2745 to 3330 cm^{-1} with a total of 115 spectral images, our equivalent spectral acquisition time increased to 920 µs per spectrum. However, depending on the application, the number of spectral points can be reconfigured dynamically for faster imaging speed, but it is beyond the scope of this manuscript. In Fig. 5(B), we can see that although the spectra of lipid droplet and the nucleolus are distinct from each other, the subtler differences between the nucleolus and cytoplasm are harder to discern. However, with the increased resolution in Fig. 5(D), we are better suited to resolve not only the fine spectral features of lipid droplets, but also those of the nucleolus and the cytoplasm. This enhanced capability should prove useful in monitoring cellular processes such as cell division, cell differentiation and apoptosis, which involve the redistribution of lipids, proteins, and nucleic acids [64,65]. Additionally, with this improved bandwidth, we start to see the detectable signal from water, which can be very useful for studying the intracellular hydrodynamics in single cells [66,67].

Biomedical Optics EXPRESS

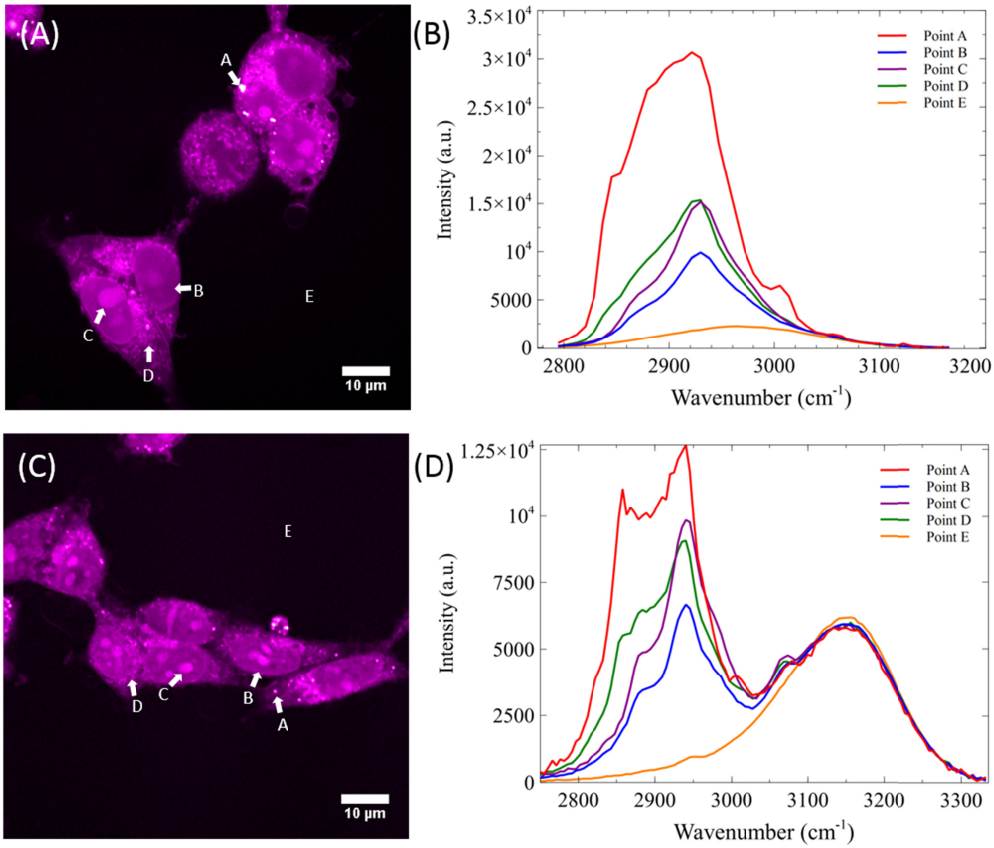

Fig. 5. (A) SRS frame at 2930 cm^{-1} of two fixed cells using unamplified Stokes pulse. (B) SRS spectra at four individual pixels A, B, C, D and E with neglible water signal in the area surrounding the fixed cells. (C) SRS frame at 2930 cm^{-1} with amplified Stokes pulse by pumping the amplifier at 2.5 W. (D) SRS spectra of four individual pixels A, B, C, D, and E. Images are acquired at 8 μs pixel dwell time. I_P and I_S = 40 mW.

To further validate the benefits of employing parabolic fiber amplifier for hsSRS imaging, we demonstrated hsSRS imaging of mammalian cells in the fingerprint region from 750 to 1700 cm^{-1}. To cover the spectral region spanning 750 to 1700 cm^{-1}, it is necessary to scan through four different wavelengths (890, 914, 935, and 951 nm) and concatenate the resulting hyperspectral data using the original laser system. As mentioned before, having to tune the laser wavelength takes several seconds and this proves inconvenient when having to tune to four different excitation wavelengths. To cover the full fingerprint region, we acquire 135 spectral images. Figure 6(A) shows a SRS frame at 1090 cm^{-1} using the glass rod setup, which shows lower signal compared to the SRS image in the high wavenumber region. To produce a SRS spectrum covering the region from 750 to 1700 cm^{-1}, the hyperspectral information generated by the pixels labeled A, B, C, and D were stitched together and shown in Fig. 6(B). As before, pixels A, B, C, and D represent the spectra of a lipid droplet, nucleus, nucleolus, and cytoplasm, respectively. We used pump excitation wavelengths of 890, 914, 935, and 951 nm to probe the regions spanning 1550 to 1700 cm^{-1}, 1200 to 1550 cm^{-1}, 955 to 1200 cm^{-1}, and 750 to 955 cm^{-1} respectively. The SRS spectral data from the few respective cellular features are shown in Fig. 6(A) and (B). The spectrum of the lipid droplet exhibits similar features to that of oleic acid as can be seen in in the region of 1200 to 1500 cm^{-1} in Fig. 6(A). This is further corroborated with the Raman transition at 1655 cm^{-1} that originates from the C = C vibrations of unsaturated lipids, which overlaps with the broader Amide I

Biomedical Optics EXPRESS

band of proteins located in the nucleus and cytoplasm (points B and C). Unfortunately, the distinction between these points is not very apparent due to the low spectral resolution afforded in this SRS configuration. In comparison, the increased bandwidth enabled by the parabolic fiber amplifier allows us to reduce the hyperspectral imaging to just two regions: 1700 – 1300 cm^{-1} and 1300 – 700 cm^{-1}. We acquired these two regions by tuning the pump excitation wavelength to 912 nm for the upper region of the fingerprint region and 949 nm for the lower part (Fig. 6(D)), with a total of 195 spectral images. SRS image at 1090 cm^{-1} with the parabolic amplifier is shown in Fig. 6(C). To compensate for the signal loss due to long Stokes pulses, we increase the Stokes power from 40 mW to 90 mW, which is still below typical values used for SRS imaging within the cell's fingerprint region [18,22,28,68,69]. The SRS spectral data from points A, B, C, and D in Fig. 6(C) are shown in Fig. 6(D). With the higher spectral resolution, the lipid droplet signal more closely resembles that of oleic acid (Fig. 3(B)). In addition, peaks originating from the nucleus and cytoplasm become more distinct and separable. These include the peak at 1004 cm^{-1} which originates from the ring-breathing mode of phenylalanine in proteins [68], the 1084 cm^{-1} peak from skeletal C-C vibrations, and the 1100 cm^{-1} peak of nucleic acids [70]. In addition, the small and sharp signal at 785 cm^{-1} originating from the symmetric phosphodiester stretch of nucleic acids further differentiates nucleus from the broad peak from lipids and proteins. These rich spectra features demonstrate that potential of parabolic amplification for broadband spectroscopic imaging across the fingerprint region.

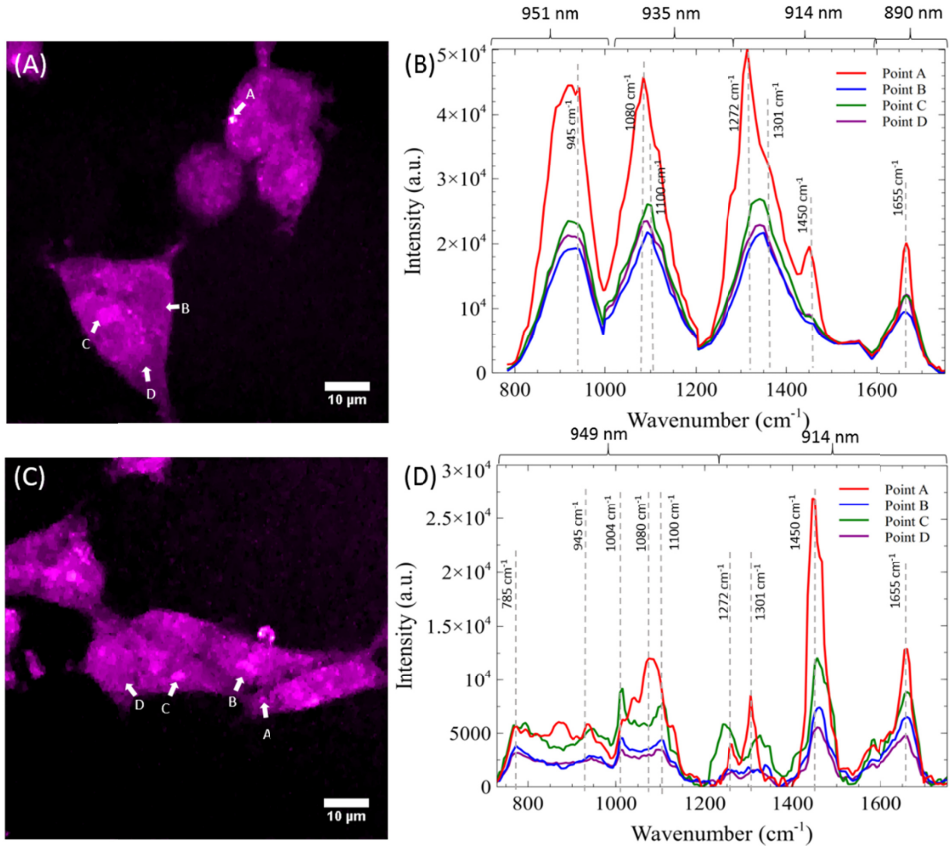

Fig. 6. (A) SRS frame at 1090 cm^{-1} of two fixed cells using unamplified Stokes pulse. (B) SRS spectra at four individual pixels A, B, C, and D. (C) SRS frame at 1090 cm^{-1} with amplified Stokes pulse by pumping the amplifier at 4.5 W. (D) SRS spectra of four individual pixels A, B, C, and D. Images are acquired at 8 μs pixel dwell time.

Biomedical Optics EXPRESS

To further demonstrate the use of broadband hsSRS in biomedical imaging, we applied our instrument to study amyloid plaques in human brains with Alzheimer's Disease. Alzheimer's disease (AD) is currently one of the most common causes of dementia and many resources are spent to improve early detection as well as mechanistic understanding of the disease. Raman spectroscopy and CARS has previously been implemented to study biochemical composition of AD plaques including Aβ peptide aggregates, fibrils, and associated lipids to characterize the effect of Alzheimer's disease on human brain tissue [71,72]. However, the low acquisition speed (50 ms/pixel) of spontaneous Raman spectroscopy and CARS (20 s/image) can be prohibitive when studying large pieces of tissue in clinical setting. Here, we exploit the benefit of broadband hsSRS over spontaneous Raman or CARS for fast, hyperspectral imaging (8 μs/pixel).

We first performed calibration studies on spectroscopic properties of insulin and insulin fibrils as a control for beta-sheets prevalent in fibril formation. Examination of the spectrum of formed fibrils showed the presence of a sharp peak around 1670 cm^{-1} (Fig. 7(A)). Using the β-sheet signatures at 1670 cm^{-1}, we were able to visualize insulin fibrils as seen in Fig. 7(B). We then proceeded to perform hsSRS imaging on a section of a superior temporal gyrus collected postmortem from a donor patient with clinically confirmed AD. Obtaining hyperspectral data for AD plaques, we were able to measure the fingerprint region of tissue and plaques. With the spectral information, the chemical composition can be extracted by employing a non-negative least squares algorithm along with the basis spectra for the individual components. Therefore, running our hsSRS imaging provides detailed chemical mapping between the uninvolved tissue and plaques, where we have determined the presence of β-sheet formation corresponding to AD plaques and neurofibrillary tangles.

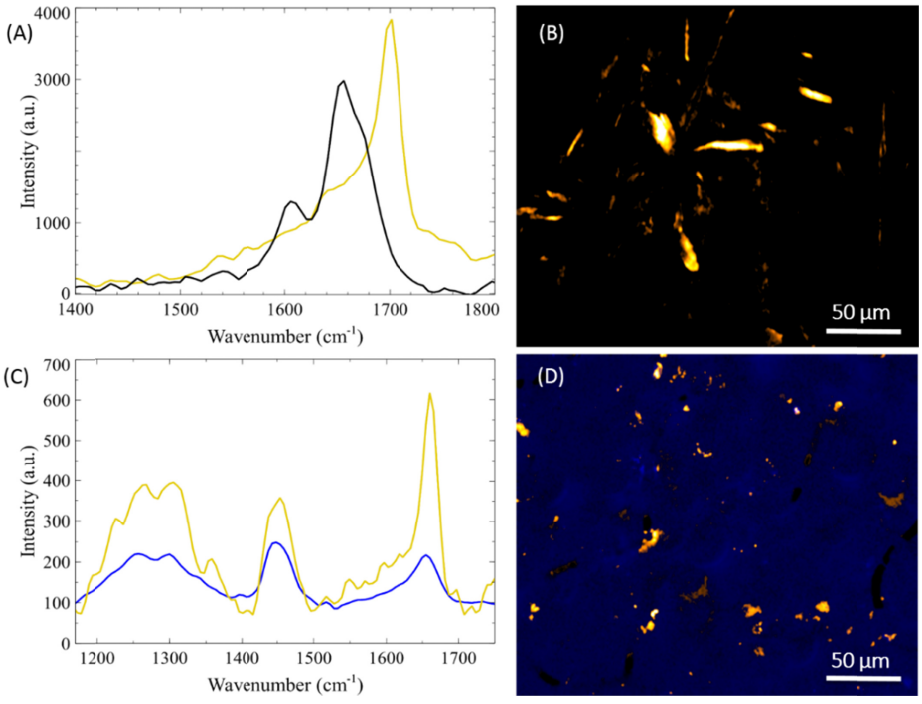

Fig. 7. (A) SRS spectra of dissolved insulin (black) and insulin fibrils (gold). (B) Hyperspectral imaging frame at 1673 cm^{-1} of insulin fibrils. (C) SRS spectra of cortex uninvolved with plaque (blue) and Aβ fibrils (gold), one of the main components of AD induced plaques. (D) Spectrally separated uninvolved tissue and plaques through a non-negative least squares algorithm. The areas of Aβ are highlighted (gold) in the background of the brain cortex (blue).

Biomedical Optics EXPRESS

Lastly, we note that although we significantly increased our hsSRS bandwidth over the previous configuration, the overall detection sensitivity decreased. This is due to a mismatch of the bandwidths which results in wasted spectral power density when matching a vibrational frequency via the spectral focusing approach. In addition, the longer pulse duration used also decreases pulse peak power with resulting lower sensitivity. However, depending on the application, if large bandwidths are not required, the spectral tunability of the parabolic amplifier allows us to produce a gain in signal by reducing the Stokes bandwidth. Here we demonstrate that the sensitivity of hsSRS imaging depends on the bandwidth of the amplified output Stokes beam. In addition to matching the chirp rates between the pump and Stokes beam, theory predicts that optimal SRS signal will be achieved when the bandwidths of both beams are approximately equal [36]. Because our tunable pump bandwidth is ~150 cm^{-1}, we expect to see highest sensitivity as the amplified Stokes bandwidth approaches the pump's bandwidth. As seen in Fig. 8, the SNR decreases linearly with increasing Stokes bandwidth. Therefore, an approximate enhancement in SNR of 2.5-fold can be achieved when the bandwidths are comparable instead of maximizing the Stokes bandwidth. The nonlinear behavior observed is due to higher order dispersion when the bandwidth is very large. Nonetheless, the decrease in sensitivity with large spectral bandwidth can be partly compensated with higher optical power due to lower photodamage from longer Stokes pulse duration. Therefore, the laser bandwidth for a particular imaging application should be chosen based on the spectral bandwidth and sensitivity required.

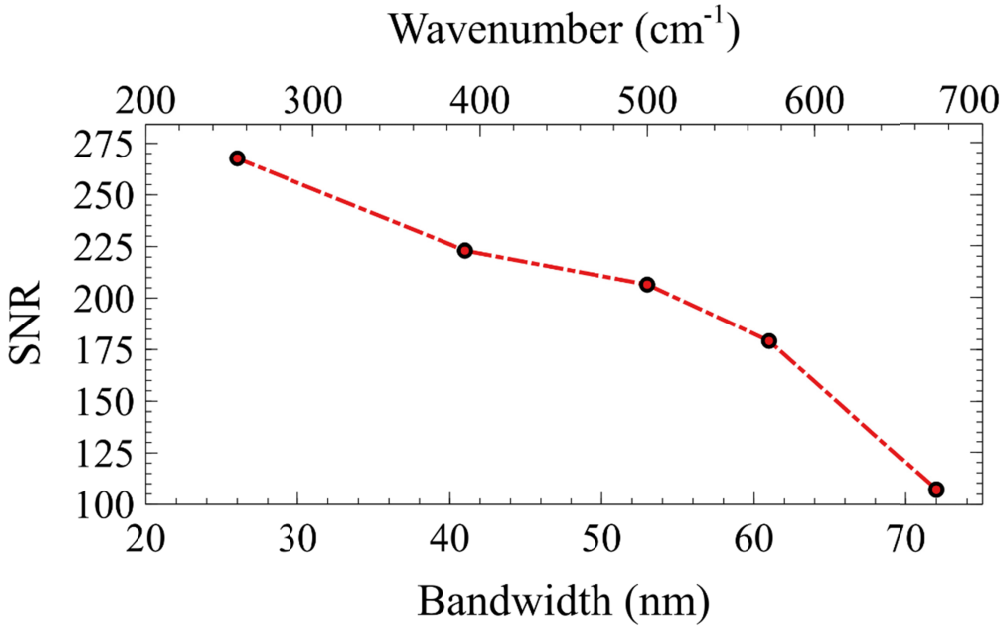

Fig. 8. Sensitivity of SRS based on parabolic pulse amplification. Images are acquired at 4 µs pixel dwell time. I_P and I_S = 15 mW.

4. Conclusion

The employment of parabolic pulse amplification provides a viable technique for increasing the bandwidth of the widely used Insight DS + laser system for hsSRS spectral coverage to a maximum of 3-fold. This technique could be useful for the spectroscopic imaging of biological cells and tissues. We showed that with spectral broadening, hsSRS imaging could cover up to ~680 cm^{-1} without the need to change wavelengths. The entire fingerprint region

Biomedical Optics EXPRESS

can be covered with two separate scans at two different pump wavelengths. In addition to increased spectral coverage, we demonstrate an improvement in spectral resolution compared to traditional spectral-focusing hsSRS setups. The resolution is currently limited to ~10 cm^{-1}, close to the natural linewidth of the Raman peak measured. It can be further improved by incorporating prism pairs or pulse shapers to correct the higher order chirp on the amplified Stokes beam. We demonstrated fast hsSRS imaging in the fingerprint region with the parabolic amplifier which offers much richer spectral features than our original SRS system. At the current stage, our data acquisition speed is mostly limited by the delay line stage movement, scanning mirrors, and software setup for a minimum pixel dwell time of 4 us. Even with an 8 us pixel dwell time that was used for imaging, the equivalent acquisition time per spectra in the fingerprint region is 1.6 ms/spectra, which enables acquisitions speeds faster than references [40] and [46], but comparable to broadband CARS imaging, which has achieved spectral acquisition time of 3.5 ms with a spectral coverage of ~425 – 2,000 cm^{-1} [12]. However, we note that quantitative spectral measurement of CARS requires phase-retrieval, and therefore it is necessary to acquire the full spectrum at high spectral resolution. In contrast, because hyperspectral SRS does not have the non-resonant background problem and the signal is strictly linearly proportional to concentration, it is not necessary to sample the entire spectrum. In fact, discrete sampling at selected wavenumbers via feature selection is more effective in quantitative analysis of a multicomponent system [73,74]. This has been illustrated in SRS imaging of nucleic acids using only three wavenumbers in the C-H region [16]. In our spectral focusing SRS configuration, discrete sampling can be readily achieved by programming delay stage positions to sequentially perform SRS imaging at predetermined wavenumbers. This will signicantly speed up SRS imaging and is a unique advantage over quantitative CARS imaging. We anticipate broad biomedical imaging applications of our proposed platform. Label-free chemical mapping of individual cells by hsSRS microscopy opens new opportunities of quantitative chemical imaging of metabolites and small molecule drugs in cells, tissues, and animals. Future studies will focus on improving spectral resolution, removing higher order chirp, improving sensitivity, and applying hsSRS imaging via parabolic pulse amplification to study lipid metabolism and tissue diagnosis.

Funding

Arnold and Mabel Beckman Foundation; UW Start-up; NIH (EB002019); NSF (GRF DGE-12560682).

Acknowledgments

We thank Drs. Gordana Juric-Sekhar and Dirk Keene for neuropathology expertise. We thank Eleanor Munger for kindly culturing the HEK293 cells and fixing the samples for imaging.

Any opinions, findings, and conclusions or recommendations expressed in this material are those of the author(s) and do not necessarily reflect the views of the National Science Foundation. Autopsy materials used in this study were obtained from the University of Washington Neuropathology Core, which is supported by the Alzheimer's Disease Research Center (AG05136) and the Adult Changes in Thought Study (AG006781).

Disclosures

The authors declare that there are no conflicts of interest related to this article.

References

1. A. S. Stender, K. Marchuk, C. Liu, S. Sander, M. W. Meyer, E. A. Smith, B. Neupane, G. Wang, J. Li, J.-X. Cheng, B. Huang, and N. Fang, "Single Cell Optical Imaging and Spectroscopy," Chem. Rev. **113**(4), 2469–2527 (2013).
2. J. W. Chan, D. S. Taylor, T. Zwerdling, S. M. Lane, K. Ihara, and T. Huser, "Micro-Raman spectroscopy detects individual neoplastic and normal hematopoietic cells," Biophys. J. **90**(2), 648–656 (2006).

Biomedical Optics EXPRESS

3. H.-J. van Manen, Y. M. Kraan, D. Roos, and C. Otto, "Single-cell Raman and fluorescence microscopy reveal the association of lipid bodies with phagosomes in leukocytes," Proc. Natl. Acad. Sci. U.S.A. **102**(29), 10159–10164 (2005).
4. J. R. Baena and B. Lendl, "Raman spectroscopy in chemical bioanalysis," Curr. Opin. Chem. Biol. **8**(5), 534–539 (2004).
5. C. L. Evans and X. S. Xie, "Coherent Anti-Stokes Raman Scattering Microscopy: Chemical Imaging for Biology and Medicine," Annu. Rev. Anal. Chem. (Palo Alto, Calif.) **1**(1), 883–909 (2008).
6. A. Zumbusch, G. R. Holtom, and X. S. Xie, "Three-Dimensional Vibrational Imaging by Coherent Anti-Stokes Raman Scattering," Phys. Rev. Lett. **82**(20), 4142–4145 (1999).
7. J.-X. Cheng and X. S. Xie, "Coherent Anti-Stokes Raman Scattering Microscopy: Instrumentation, Theory, and Applications," J. Phys. Chem. B **108**(3), 827–840 (2004).
8. C. H. Camp, Jr., Y. J. Lee, and M. T. Cicerone, "Quantitative, comparable coherent anti-Stokes Raman scattering (CARS) spectroscopy: correcting errors in phase retrieval," J. Raman Spectrosc. **47**(4), 408–415 (2016).
9. J. P. R. Day, K. F. Domke, G. Rago, H. Kano, H. O. Hamaguchi, E. M. Vartiainen, and M. Bonn, "Quantitative Coherent Anti-Stokes Raman Scattering (CARS) Microscopy," J. Phys. Chem. B **115**(24), 7713–7725 (2011).
10. M. T. Cicerone, K. A. Aamer, Y. J. Lee, and E. Vartiainen, "Maximum entropy and time-domain Kramers–Kronig phase retrieval approaches are functionally equivalent for CARS microspectroscopy," J. Raman Spectrosc. **43**(5), 637–643 (2012).
11. E. M. Vartiainen, H. A. Rinia, M. Müller, and M. Bonn, "Direct extraction of Raman line-shapes from congested CARS spectra," Opt. Express **14**(8), 3622–3630 (2006).
12. C. H. Camp, Jr., Y. J. Lee, J. M. Heddleston, C. M. Hartshorn, A. R. Hight Walker, J. N. Rich, J. D. Lathia, and M. T. Cicerone, "High-speed coherent Raman fingerprint imaging of biological tissues," Nat. Photonics **8**(8), 627–634 (2014).
13. D. Fu, "Quantitative chemical imaging with stimulated Raman scattering microscopy," Curr. Opin. Chem. Biol. **39**, 24–31 (2017).
14. J.-X. Cheng and X. S. Xie, "Vibrational spectroscopic imaging of living systems: An emerging platform for biology and medicine," Science **350**(6264), aaa8870 (2015).
15. C. W. Freudiger, W. Min, B. G. Saar, S. Lu, G. R. Holtom, C. He, J. C. Tsai, J. X. Kang, and X. S. Xie, "Label-free biomedical imaging with high sensitivity by stimulated Raman scattering microscopy," Science **322**(5909), 1857–1861 (2008).
16. F.-K. Lu, S. Basu, V. Igras, M. P. Hoang, M. Ji, D. Fu, G. R. Holtom, V. A. Neel, C. W. Freudiger, D. E. Fisher, and X. S. Xie, "Label-free DNA imaging in vivo with stimulated Raman scattering microscopy," Proc. Natl. Acad. Sci. U.S.A. **112**(37), 11624–11629 (2015).
17. C. H. Camp, Jr. and M. T. Cicerone, "Chemically sensitive bioimaging with coherent Raman scattering," Nat. Photonics **9**(5), 295–305 (2015).
18. M. Ji, D. A. Orringer, C. W. Freudiger, S. Ramkissoon, X. Liu, D. Lau, A. J. Golby, I. Norton, M. Hayashi, N. Y. R. Agar, G. S. Young, C. Spino, S. Santagata, S. Camelo-Piragua, K. L. Ligon, O. Sagher, and X. S. Xie, "Rapid, Label-Free Detection of Brain Tumors with Stimulated Raman Scattering Microscopy," Sci. Transl. Med. **5**(201), 201ra119 (2013).
19. J.-X. Cheng and X. S. Xie, *Coherent Raman Scattering Microscopy* (CRC Press, 2017).
20. W. J. Tipping, M. Lee, A. Serrels, V. G. Brunton, and A. N. Hulme, "Stimulated Raman scattering microscopy: an emerging tool for drug discovery," Chem. Soc. Rev. **45**(8), 2075–2089 (2016).
21. W. Min, C. W. Freudiger, S. Lu, and X. S. Xie, "Coherent Nonlinear Optical Imaging: Beyond Fluorescence Microscopy," Annu. Rev. Phys. Chem. **62**(1), 507–530 (2011).
22. D. A. Orringer, B. Pandian, Y. S. Niknafs, T. C. Hollon, J. Boyle, S. Lewis, M. Garrard, S. L. Hervey-Jumper, H. J. L. Garton, C. O. Maher, J. A. Heth, O. Sagher, D. A. Wilkinson, M. Snuderl, S. Venneti, S. H. Ramkissoon, K. A. McFadden, A. Fisher-Hubbard, A. P. Lieberman, T. D. Johnson, X. S. Xie, J. K. Trautman, C. W. Freudiger, and S. Camelo-Piragua, "Rapid intraoperative histology of unprocessed surgical specimens via fibre-laser-based stimulated Raman scattering microscopy," Nat. Biomed. Eng. **1**(2), 0027 (2017).
23. M. Ji, S. Lewis, S. Camelo-Piragua, S. H. Ramkissoon, M. Snuderl, S. Venneti, A. Fisher-Hubbard, M. Garrard, D. Fu, A. C. Wang, J. A. Heth, C. O. Maher, N. Sanai, T. D. Johnson, C. W. Freudiger, O. Sagher, X. S. Xie, and D. A. Orringer, "Detection of human brain tumor infiltration with quantitative stimulated Raman scattering microscopy," Sci. Transl. Med. **7**(309), 309ra163(2015).
24. F.-K. Lu, D. Calligaris, O. I. Olubiyi, I. Norton, W. Yang, S. Santagata, X. S. Xie, A. J. Golby, and N. Y. R. Agar, "Label-Free Neurosurgical Pathology with Stimulated Raman Imaging," Cancer Res. **76**(12), 3451–3462 (2016).
25. J. Li, S. Condello, J. Thomes-Pepin, X. Ma, Y. Xia, T. D. Hurley, D. Matei, and J.-X. Cheng, "Lipid Desaturation Is a Metabolic Marker and Therapeutic Target of Ovarian Cancer Stem Cells," Cell Stem Cell **20**(3), 303–314 (2017).
26. S. Yue and J.-X. Cheng, "Deciphering Single Cell Metabolism by Coherent Raman Scattering Microscopy," Curr. Opin. Chem. Biol. **33**, 46–57 (2016).
27. D. Fu, J. Zhou, W. S. Zhu, P. W. Manley, Y. K. Wang, T. Hood, A. Wylie, and X. S. Xie, "Imaging the intracellular distribution of tyrosine kinase inhibitors in living cells with quantitative hyperspectral stimulated Raman scattering," Nat. Chem. **6**(7), 614–622 (2014).

Biomedical Optics EXPRESS

28. L. Wei, F. Hu, Y. Shen, Z. Chen, Y. Yu, C.-C. Lin, M. C. Wang, and W. Min, "Live-cell imaging of alkyne-tagged small biomolecules by stimulated Raman scattering," Nat. Methods **11**(4), 410–412 (2014).
29. F. Hu, Z. Chen, L. Zhang, Y. Shen, L. Wei, and W. Min, "Vibrational Imaging of Glucose Uptake Activity in Live Cells and Tissues by Stimulated Raman Scattering," Angew. Chem. Int. Ed. Engl. **54**(34), 9821–9825 (2015).
30. J. M. Crawford, C. Portmann, X. Zhang, M. B. J. Roeffaers, and J. Clardy, "Small molecule perimeter defense in entomopathogenic bacteria," Proc. Natl. Acad. Sci. U.S.A. **109**(27), 10821–10826 (2012).
31. S. Hong, T. Chen, Y. Zhu, A. Li, Y. Huang, and X. Chen, "Live-Cell Stimulated Raman Scattering Imaging of Alkyne-Tagged Biomolecules," Angew. Chem. Int. Ed. Engl. **53**(23), 5827–5831 (2014).
32. D. Fu, F.-K. Lu, X. Zhang, C. Freudiger, D. R. Pernik, G. Holtom, and X. S. Xie, "Quantitative Chemical Imaging with Multiplex Stimulated Raman Scattering Microscopy," J. Am. Chem. Soc. **134**(8), 3623–3626 (2012).
33. D. Zhang, P. Wang, M. N. Slipchenko, D. Ben-Amotz, A. M. Weiner, and J.-X. Cheng, "Quantitative Vibrational Imaging by Hyperspectral Stimulated Raman Scattering Microscopy and Multivariate Curve Resolution Analysis," Anal. Chem. **85**(1), 98–106 (2013).
34. Y. Ozeki, W. Umemura, K. Sumimura, N. Nishizawa, K. Fukui, and K. Itoh, "Stimulated Raman hyperspectral imaging based on spectral filtering of broadband fiber laser pulses," Opt. Lett. **37**(3), 431–433 (2012).
35. E. R. Andresen, P. Berto, and H. Rigneault, "Stimulated Raman scattering microscopy by spectral focusing and fiber-generated soliton as Stokes pulse," Opt. Lett. **36**(13), 2387–2389 (2011).
36. D. Fu, G. Holtom, C. Freudiger, X. Zhang, and X. S. Xie, "Hyperspectral Imaging with Stimulated Raman Scattering by Chirped Femtosecond Lasers," J. Phys. Chem. B **117**(16), 4634–4640 (2013).
37. J. L. Suhalim, C.-Y. Chung, M. B. Lilledahl, R. S. Lim, M. Levi, B. J. Tromberg, and E. O. Potma, "Characterization of Cholesterol Crystals in Atherosclerotic Plaques Using Stimulated Raman Scattering and Second-Harmonic Generation Microscopy," Biophys. J. **102**(8), 1988–1995 (2012).
38. C.-S. Liao, M. N. Slipchenko, P. Wang, J. Li, S.-Y. Lee, R. A. Oglesbee, and J.-X. Cheng, "Microsecond scale vibrational spectroscopic imaging by multiplex stimulated Raman scattering microscopy," Light Sci. Appl. **4**(3), e265 (2015).
39. J. Réhault, F. Crisafi, V. Kumar, G. Ciardi, M. Marangoni, G. Cerullo, and D. Polli, "Broadband stimulated Raman scattering with Fourier-transform detection," Opt. Express **23**(19), 25235–25246 (2015).
40. T. Hellerer, A. M. K. Enejder, and A. Zumbusch, "Spectral focusing: High spectral resolution spectroscopy with broad-bandwidth laser pulses," Appl. Phys. Lett. **85**(1), 25–27 (2004).
41. H. T. Beier, G. D. Noojin, and B. A. Rockwell, "Stimulated Raman scattering using a single femtosecond oscillator with flexibility for imaging and spectral applications," Opt. Express **19**(20), 18885–18892 (2011).
42. A. F. Pegoraro, A. Ridsdale, D. J. Moffatt, Y. Jia, J. P. Pezacki, and A. Stolow, "Optimally chirped multimodal CARS microscopy based on a single Ti:sapphire oscillator," Opt. Express **17**(4), 2984–2996 (2009).
43. I. Rocha-Mendoza, W. Langbein, and P. Borri, "Coherent anti-Stokes Raman microspectroscopy using spectral focusing with glass dispersion," Appl. Phys. Lett. **93**(20), 201103 (2008).
44. A. F. Pegoraro, A. D. Slepkov, A. Ridsdale, D. J. Moffatt, and A. Stolow, "Hyperspectral multimodal CARS microscopy in the fingerprint region," J. Biophotonics **7**(1-2), 49–58 (2014).
45. W. Langbein, I. Rocha-Mendoza, and P. Borri, "Coherent anti-Stokes Raman micro-spectroscopy using spectral focusing: theory and experiment," J. Raman Spectrosc. **40**(7), 800–808 (2009).
46. B. Figueroa, Y. Chen, K. Berry, A. Francis, and D. Fu, "Label-Free Chemical Imaging of Latent Fingerprints with Stimulated Raman Scattering Microscopy," Anal. Chem. **89**(8), 4468–4473 (2017).
47. B. Liu, H. J. Lee, D. Zhang, C.-S. Liao, N. Ji, Y. Xia, and J.-X. Cheng, "Label-free spectroscopic detection of membrane potential using stimulated Raman scattering," Appl. Phys. Lett. **106**(17), 173704 (2015).
48. S. Karpf, M. Eibl, W. Wieser, T. Klein, and R. Huber, "A Time-Encoded Technique for fibre-based hyperspectral broadband stimulated Raman microscopy," Nat. Commun. **6**(1), 6784 (2015).
49. R. Paschotta, J. Nilsson, A. C. Tropper, and D. C. Hanna, "Ytterbium-doped fiber amplifiers," IEEE J. Quantum Electron. **33**(7), 1049–1056 (1997).
50. M. E. Fermann, V. I. Kruglov, B. C. Thomsen, J. M. Dudley, and J. D. Harvey, "Self-Similar Propagation and Amplification of Parabolic Pulses in Optical Fibers," Phys. Rev. Lett. **84**(26), 6010–6013 (2000).
51. V. I. Kruglov, A. C. Peacock, J. M. Dudley, and J. D. Harvey, "Self-similar propagation of high-power parabolic pulses in optical fiber amplifiers," Opt. Lett. **25**(24), 1753–1755 (2000).
52. V. I. Kruglov, A. C. Peacock, J. D. Harvey, and J. M. Dudley, "Self-similar propagation of parabolic pulses in normal-dispersion fiber amplifiers," J. Opt. Soc. Am. B **19**(3), 461–469 (2002).
53. C. Finot, J. M. Dudley, B. Kibler, D. J. Richardson, and G. Millot, "Optical Parabolic Pulse Generation and Applications," IEEE J. Quantum Electron. **45**(11), 1482–1489 (2009).
54. A. C. Peacock, R. J. Kruhlak, J. D. Harvey, and J. M. Dudley, "Solitary pulse propagation in high gain optical fiber amplifiers with normal group velocity dispersion," Opt. Commun. **206**(1), 171–177 (2002).
55. D. B. Soh, J. Nilsson, and A. B. Grudinin, "Efficient femtosecond pulse generation using a parabolic amplifier combined with a pulse compressor I Stimulated Raman-scattering effects," J. Opt. Soc. Am. B **23**(1), 1 (2006).
56. D. B. Soh, J. Nilsson, and A. B. Grudinin, "Efficient femtosecond pulse generation using a parabolic amplifier combined with a pulse compressor. II. Finite gain-bandwidth effect," J. Opt. Soc. Am. B **23**(1), 10–19 (2006).
57. Y. Deng, C.-Y. Chien, B. G. Fidric, and J. D. Kafka, "Generation of sub-50 fs pulses from a high-power Yb-doped fiber amplifier," Opt. Lett. **34**(22), 3469–3471 (2009).

Biomedical Optics EXPRESS

58. J. Limpert, T. Schreiber, T. Clausnitzer, K. Zöllner, H. Fuchs, E. Kley, H. Zellmer, and A. Tünnermann, "High-power femtosecond Yb-doped fiber amplifier," Opt. Express **10**(14), 628–638 (2002).
59. A. Francis, K. Berry, Y. Chen, B. Figueroa, and D. Fu, "Label-free pathology by spectrally sliced femtosecond stimulated Raman scattering (SRS) microscopy," PLoS One **12**(5), e0178750 (2017).
60. M. Lai, S. T. Lai, and C. Swinger, "Single-grating laser pulse stretcher and compressor," Appl. Opt. **33**(30), 6985–6987 (1994).
61. M. Pessot, P. Maine, and G. Mourou, "1000 times expansion/compression of optical pulses for chirped pulse amplification," Opt. Commun. **62**(6), 419–421 (1987).
62. G. Chang, A. Galvanauskas, H. G. Winful, and T. B. Norris, "Dependence of parabolic pulse amplification on stimulated Raman scattering and gain bandwidth," Opt. Lett. **29**(22), 2647–2649 (2004).
63. D. N. Papadopoulos, Y. Zaouter, M. Hanna, F. Druon, E. Mottay, E. Cormier, and P. Georges, "Generation of 63 fs 4.1 MW peak power pulses from a parabolic fiber amplifier operated beyond the gain bandwidth limit," Opt. Lett. **32**(17), 2520–2522 (2007).
64. N. Uzunbajakava, A. Lenferink, Y. Kraan, E. Volokhina, G. Vrensen, J. Greve, and C. Otto, "Nonresonant Confocal Raman Imaging of DNA and Protein Distribution in Apoptotic Cells," Biophys. J. **84**(6), 3968–3981 (2003).
65. G. J. Puppels, F. F. M. de Mul, C. Otto, J. Greve, M. Robert-Nicoud, D. J. Arndt-Jovin, and T. M. Jovin, "Studying single living cells and chromosomes by confocal Raman microspectroscopy," Nature **347**(6290), 301–303 (1990).
66. E. Potma, W. P. de Boeij, P. J. M. van Haastert, and D. A. Wiersma, "Real-time visualization of intracellular hydrodynamics in single living cells," Proc. Natl. Acad. Sci. U.S.A. **98**(4), 1577–1582 (2001).
67. J.-X. Cheng, S. Pautot, D. A. Weitz, and X. S. Xie, "Ordering of water molecules between phospholipid bilayers visualized by coherent anti-Stokes Raman scattering microscopy," Proc. Natl. Acad. Sci. U.S.A. **100**(17), 9826–9830 (2003).
68. X. Zhang, M. B. J. Roeffaers, S. Basu, J. R. Daniele, D. Fu, C. W. Freudiger, G. R. Holtom, and X. S. Xie, "Label-free Live-Cell Imaging of Nucleic Acids using Stimulated Raman Scattering Microscopy," ChemPhysChem **13**(4), 1054–1059 (2012).
69. C. W. Freudiger, W. Min, G. R. Holtom, B. Xu, M. Dantus, and X. S. Xie, "Highly specific label-free molecular imaging with spectrally tailored excitation stimulated Raman scattering (STE-SRS) microscopy," Nat. Photonics **5**(2), 103–109 (2011).
70. D. C. Goodwin and J. Brahms, "Form of DNA and the nature of interactions with proteins in chromatin," Nucleic Acids Res. **5**(3), 835–850 (1978).
71. R. Michael, A. Lenferink, G. F. J. M. Vrensen, E. Gelpi, R. I. Barraquer, and C. Otto, "Hyperspectral Raman imaging of neuritic plaques and neurofibrillary tangles in brain tissue from Alzheimer's disease patients," Sci. Rep. **7**(1), 15603 (2017).
72. J. Kiskis, H. Fink, L. Nyberg, J. Thyr, J.-Y. Li, and A. Enejder, "Plaque-associated lipids in Alzheimer's diseased brain tissue visualized by nonlinear microscopy," Sci. Rep. **5**(1), 13489 (2015).
73. L. Yi-Zeng, X. Yu-Long, and Y. Ru-Qin, "Accuracy criteria and optimal wavelength selection for multicomponent spectrophotometric determinations," Anal. Chim. Acta **222**(1), 347–357 (1989).
74. D. Fu and X. S. Xie, "Reliable Cell Segmentation Based on Spectral Phasor Analysis of Hyperspectral Stimulated Raman Scattering Imaging Data," Anal. Chem. **86**(9), 4115–4119 (2014).